ORIGINAL PAPER

Transparent conducting Sn:ZnO films deposited from nanoparticles

Li Luo · Kathrin Häfliger · Dan Xie · Markus Niederberger

Abstract Homogeneous transparent conducting Sn:ZnO films on fused silica substrates were prepared by dip-coating from nanoparticle dispersions, while the nanocrystalline Sn:ZnO particles with different dopant concentrations were synthesized by microwave-assisted non-aqueous sol–gel process using Sn(IV) tert-butoxide and Zn(II) acetate as precursors and benzyl alcohol as solvent. The dopant concentration had a great impact on the electrical properties of the films. A minimum resistivity of 20.3 Ω cm was obtained for a porous Sn:ZnO film with initial Sn concentration of 7.5 mol% after annealing in air and post-annealing in N_2 at 600 °C. The resistivity of this porous film could further be reduced to 2.6 and 0.6 Ω cm after densified in Sn:ZnO and Al:ZnO reaction solution, respectively. The average optical transmittance of a 400-nm-thick Sn:ZnO film densified with Sn:ZnO after the two annealing steps was 91%.

Keywords Transparent conducting films · Sn:ZnO · Nanoparticles · Microwave-assisted nonaqueous synthesis

1 Introduction

Transparent conducting oxide (TCO) films show a high optical transmittance in the visible region as well as high electrical conductivity. This unique combination makes TCO films ideal for applications in many current and emerging optoelectronic devices, for example, gas sensors [1–3], touch-panel displays [4], liquid crystal displays (LCD) [5], organic light-emitting diodes (OLED) [6–10], smart windows [11] and solar cells [12–14]. TCOs such as $Sn:In_2O_3$ (ITO) and Al:ZnO (AZO) are well established on an industrial scale. However, the price of indium is increasing due to the rapidly growing demand of ITO, and AZO, although much cheaper than ITO, has the disadvantage of being chemically rather instable, especially in humid environment [15]. The combination of metal ions in the oxidation state 2+ and 3+ with CO_2 and water tends to form hydrated hydroxy carbonate species [16]. Therefore, it is crucial to find dopants for ZnO with other oxidation states than 3+ [17].

Various methods for TCO film deposition have been reported in the literature, such as pulsed laser deposition (PLD) [18], sputtering [19], thermal evaporation [20], spray pyrolysis [21], sol–gel technique [17, 22, 23], and chemical deposition [24]. Currently, most industrially applied techniques are physical deposition methods resulting in high quality films, however with the disadvantage that the technology is difficult to be optimized further. Moreover, they are expensive due to the high vacuum needed during the deposition of the films and the frequently required cleaning procedure of the deposition chambers. Hence, developing of low cost methods like the sol–gel technique, which have by far not yet reached the technological limit, attracts more and more interest in industry.

The conventional aqueous sol–gel process often leads to films with low crystallinity. Therefore, modified sol–gel processes for TCO films were studied in the past to improve the conductivity, for example, by preparing ITO films from preformed nanoparticle dispersions [25]. In this work, a film deposition process for Sn:ZnO films using a combination of the microwave-assisted nonaqueous sol–gel

L. Luo · K. Häfliger · D. Xie · M. Niederberger (✉)
Department of Materials, ETH Zurich, Wolfgang-Pauli-Strasse 10, Zurich, Switzerland
e-mail: markus.niederberger@mat.ethz.ch

process [26, 27] with dip-coating was developed. First, Sn:ZnO nanoparticles were synthesized by the microwave method, and then films were dip-coated on substrates from nanoparticle dispersions. The main advantages of this process are: (1) phase-pure nanoparticles with high crystallinity and narrow particle size distributions can be obtained in just a few minutes, (2) the composition of the material can be well controlled, (3) multi-component films can be achieved easily, and (4) there is almost no waste of raw material. Previous studies in the Sn–Zn–O system for TCO films by sol–gel process were mainly focused on amorphous materials [17, 28].

2 Experimental

2.1 Materials

Sn(IV) tert-butoxide $\geq$ 99.99%, Zn(II) acetate $\geq$ 99.9%, Al(III) isopropoxide $\geq$ 99.99%, benzyl alcohol $\geq$ 99.8%, cyclohexane $\geq$ 99.8%, and oleylamine were purchased from Sigma-Aldrich, and oleic acid $\geq$ 99.0% from Fluka. All chemicals were used as received.

2.2 Synthesis and dispersion

Sn:ZnO nanoparticles were synthesized using a microwave-assisted non-aqueous sol–gel method. In a glovebox with Ar atmosphere, Sn(IV) tert-butoxide was added to a 10 ml vessel according to the desired doping level (Sn/(Sn + Zn) from 0 to 20 mol%). Then, Zn(II) acetate was added to reach 1 mmol of precursors. The error of initial weighing was kept between $\pm$0.2 mg. Afterwards 5 ml benzyl alcohol was added, and the vessel was sealed with a Teflon cap and taken out of the glovebox. The reaction mixture was heated by microwave irradiation (CEM Discover reactor operating at a frequency of 2.45 GHz) at 200 °C for 3 min with high stirring. The precipitate was separated from the liquid phase by centrifugation. For characterization of nanoparticles, the precipitate was washed with ethanol and dried at 60 °C; for dispersion and film preparation, the wet powder was collected without washing.

The dispersion was produced by adding the wet powder to a mixture of cyclohexane and a surfactant. The ratio of cyclohexane to surfactant was set to 100:1 (volume). Oleic acid and oleylamine were used as surfactants. The surfactant composition has been optimized for each doping level. The ratio of oleic acid to oleylamine was 0:5 for 0%, 2:3 for 2%, 1:1 for 5%, 3:2 for 7.5% and 10%, and 5:0 for 20% of Sn. For lower doping levels a higher content of oleylamine was better, whereas for higher dopant concentrations

oleic acid alone worked best. The solid concentration of the dispersion was 43 $\pm$ 0.6 g/l.

2.3 Film preparation

A film was prepared on a fused silica substrate cleaned by ethanol using repeated dip-coating from the dispersion under ambient atmosphere. The down speed was set at 60 mm/min and withdrawal speed was 15 mm/min. After each dip the films were heat-treated in air at 300 °C for 10 min in a preheated furnace. After depositing five to ten layers, the films were then annealed in air at 600 °C for 2 h, followed by naturally cooling down to room temperature and then by annealing in nitrogen at 600 °C for another 2 h. The ramping temperature was set to 3 °C/min. To densify the films annealed in air only, they were immersed into the reaction solution, and the microwave-assisted reaction was repeated. In addition to Sn:ZnO, also Al: ZnO reaction solution was used to densify the film. The preparation of Al: ZnO reaction solution is similar to that of Sn:ZnO, only Al(III) isopropoxide (10 mol%) was used instead of Sn(IV) tert-butoxide. Afterwards, the so-densified films were annealed again at 600 °C in air and N$_2$.

2.4 Characterization

The powder X-ray diffraction (PXRD) patterns were measured in reflection mode and in θ–2θ geometry with Cu Kα radiation on a Philips diffractometer PW1800 equipped with a secondary monochromator. The high temperature XRD (HTXRD) patterns were measured in reflection mode and in θ–2θ geometry with Cu Kα radiation on a PANalytical X'Pert Pro equipped with a high temperature chamber (HTK 1200, Anton Paar). The Rietveld refinement was performed using the program *TOPAS*-Academic V4.1 [29]. The peak shape function used to fit the patterns is the modified Thompson-Cox-Hastings pseudo-Voigt function [30]. Peak asymmetry due to axial divergence was calculated by the model proposed by Finger et al. [31]. Linear absorption coefficient was used for adjusting the peak shape due to sample transparency. The preferred orientation correction was performed based on the March-Dollase model [32]. The Double-Voigt approach [33] was used to model the microstructure (size and strain) effects and calculate the volume-weighted domain size (D_V). The relationship between D_V and the average radius D of particles is not linear, a simplified expression, $D = 4/3 D_V$, proposed by Balzar [34] can be used for a monodisperse spherical system. A potential source of error in reflection geometry (Bragg–Brentano geometry) is that of surface roughness [35], therefore correction suggested by Pitschke et al. [36] was applied during the refinement.

The microstructure and thickness of the films were characterized using scanning electron microscopy (SEM, Carl Zeiss LEO 1530) equipped with a field emission gun operated at 5 kV. The surfaces of the films were sputter-coated with a platinum layer to reduce any charge effect. The final dopant concentration was analyzed by wavelength dispersive X-ray spectroscopy (WDX) at beam energy of 20 keV on a high resolution Hitachi SEM.

The UV–Vis reflection spectra of the powders were measured on a JASCO V-670 spectrophotometer with ILN-725 integrating sphere, while the transmission spectra of the films were measured with standard mode. The band gaps of the samples were determined from the reflectance of the powder, which has been proven to be a standard technique [37–39].

The electrical properties of the films were measured at room temperature using Van der Pauw method on a Hall Effect measurement system (Ecopia HMS-3000) with a 0.55 Tesla magnet kit. The film was cut into a squared piece with a size of 10×10 mm and contacted to the measurement template with metallic indium.

3 Results and discussion

3.1 Structure properties

The influence of the dopant concentration on the structure, optical and electrical properties of the Sn:ZnO nanoparticles and films were investigated. The initial dopant concentration was varied in the range 0–20 mol%. The final dopant concentration was analyzed by WDX and Rietveld refinement. The results are summarized in Table 1. Although the final dopant concentration increased with increasing initial concentration, the incorporation of the dopant is not quantitatively and the final concentration is significantly lower than the initial one. We assume that this discrepancy is partly due to the fact that a significant amount of Sn(IV) tert-butoxide remains unreacted in
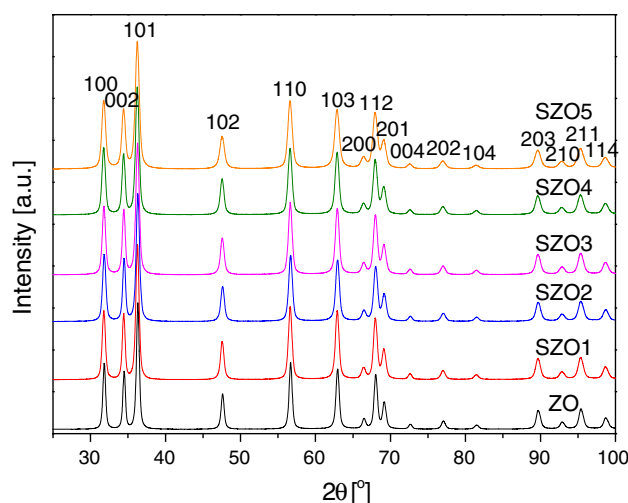

Fig. 1 PXRD patterns of Sn:ZnO nanoparticles with different initial dopant concentrations

benzyl alcohol at such low synthesis temperature and is simply washed away during product separation.

Figure 1 shows the PXRD patterns of Sn:ZnO nanoparticles with different dopant concentrations. All samples maintained the wurtzite *hcp* structure of ZnO without detectable impurities. The PXRD patterns exhibit an increase of the full width at half maximum (FWHM) of the diffraction peaks with increasing Sn concentration, pointing to a decrease of the crystallite size upon incorporation of the dopant and/or an increase of the microstrain. The observation that doping alters the crystal size can be explained by the fact that the surface energy is dependent on the dopant and its concentration [40].

The average particle size and the lattice parameters were analyzed by the Rietveld method from X-ray data. All the results are summarized in Table 1. For the undoped ZnO nanoparticles, the lattice parameters are $a = 3.2498$ and $c = 5.2071$ Å, agreeing well with the reported values of 3.2498 and 5.2066 Å (ICDD PDF No. 36-1451). The lattice parameters a and c of Sn:ZnO increased with increasing dopant concentrations, indicating that some of

Table 1 The dopant concentrations, particle sizes and lattice constants of Sn:ZnO nanoparticles

Sample ID	Initial Sn/(Sn + Zn) [mol%]	WDX Sn/(Sn + Zn) [at%]	Rietveld refinement			
			Sn/(Sn + Zn) [at%]	D [nm]	Lattice constant	
					a [Å]	c [Å]
ZO	0	0	0	22.8 (7)	3.2498(1)	5.2071(1)
SZO1	2	0.412 (±0.167)	0.4(8)	19.2 (4)	3.2509(3)	5.2086(4)
SZO2	5	0.724 (±0.279)	0.5(4)	18.4 (2)	3.2512(1)	5.2089(1)
SZO3	7.5	0.840 (±0.185)	1.0(4)	18.2 (3)	3.2511(1)	5.2090(1)
SZO4	10	0.921 (±0.149)	1.5(4)	17.1 (2)	3.2512(2)	5.2085(3)
SZO5	20	0.999 (±0.086)	1.4(4)	14.8 (3)	3.2520(1)	5.2105(2)

Table 2 Description of the film ID

Film ID	Description
SZO(1-5)F	As dip-coated SZO(1-5) films heated at 300 °C
SZO(1-5)FA	SZO(1-5) films annealed at 600 °C in air and N_2
SZO3F-D1	SZO3F (additionally annealed at 600 °C in air) densified with SZO3 reaction solution and annealed at 600 °C in air and N_2
SZO3F-D2	SZO3F (additionally annealed at 600 °C in air) densified with Al:ZnO reaction solution and annealed at 600 °C in air and N_2
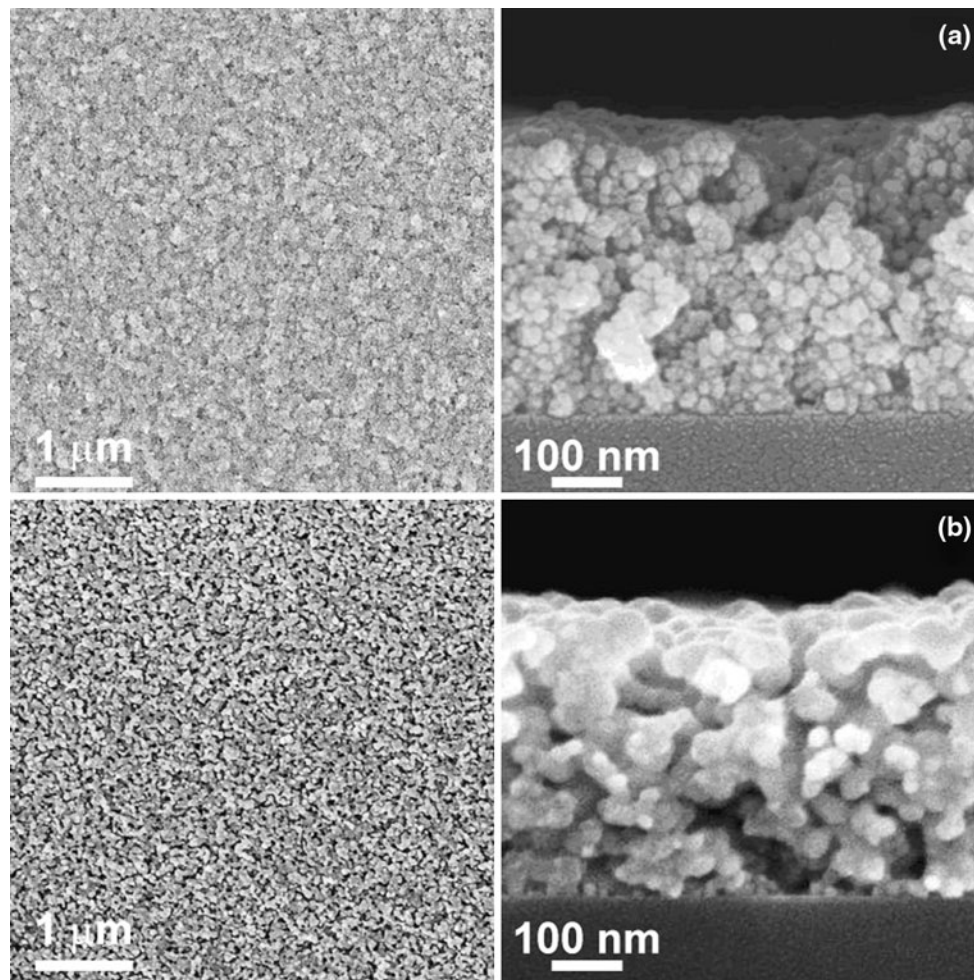
Fig. 2 SEM images of the surface (*left*) and cross section (*right*) of **a** SZO3F and **b** SZO3FA

the Sn atoms may locate on the interstitial position and/or the ionic radius of Sn^{4+} might be larger than that of Zn^{2+} (0.74 Å for 4-coordinate) [41], which means that the coordination number of Sn^{4+} in the crystal would be higher than 4 (0.69 Å for 4-coordinate, 0.83 Å for 6-coordinate, 0.95 Å for 8-coordinate) [41].

To check the phase stability at elevated temperatures, HTXRD patterns were measured as well. The phase was stable up to 600 °C for 4 h, but the crystallites grew from 18 to 40 nm. Therefore, the annealing process of the films was performed at 600 °C to avoid any phase changes.

The surface morphology and the cross-sectional microstructure of Sn:ZnO films were analyzed by SEM. The description of the different films is summarized in Table 2. As an example, Fig. 2 shows the SEM images of (Fig. 2a) SZO3F and (Fig. 2b) SZO3FA. The surface of the as-dip-coated film is homogeneous over a large area, and the thickness of the film can be tuned by varying the number of dipping times. After annealing, both the particles and the pores grew. To densify the porous film, a microwave-assisted reaction solution densification step was applied. Figure 3 shows the SEM images of SZO3FA film densified
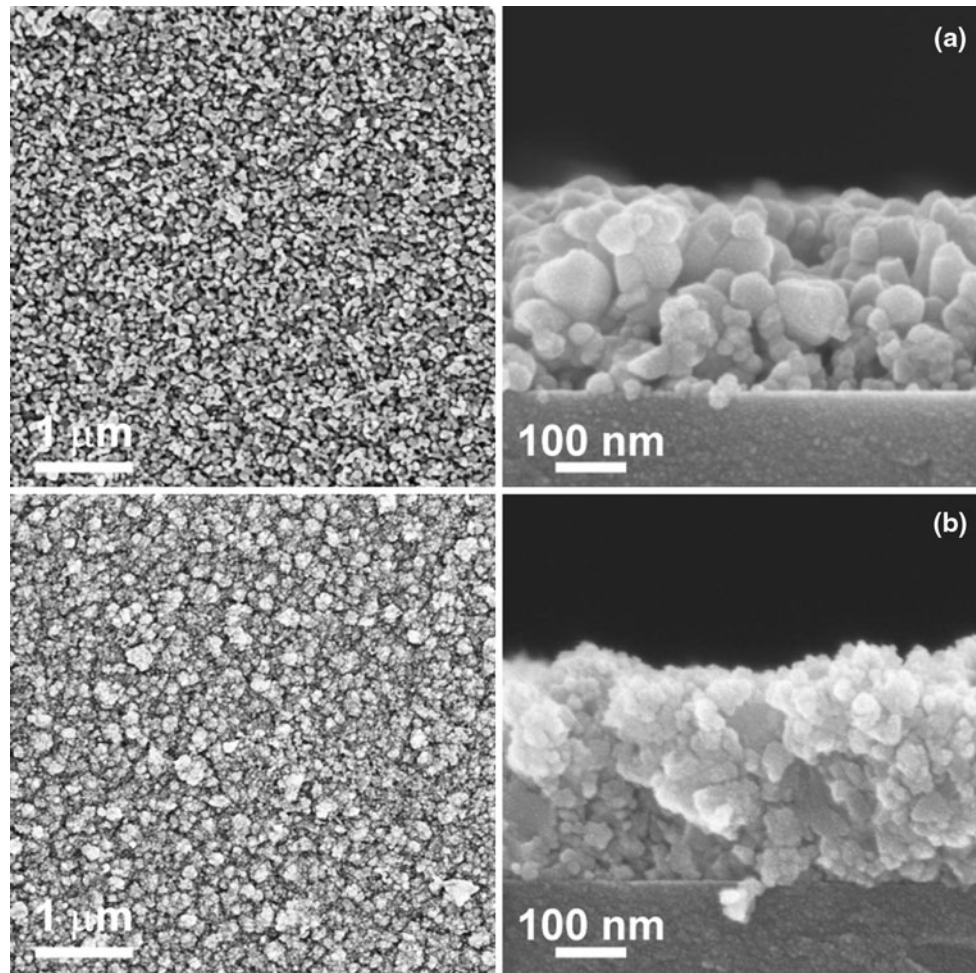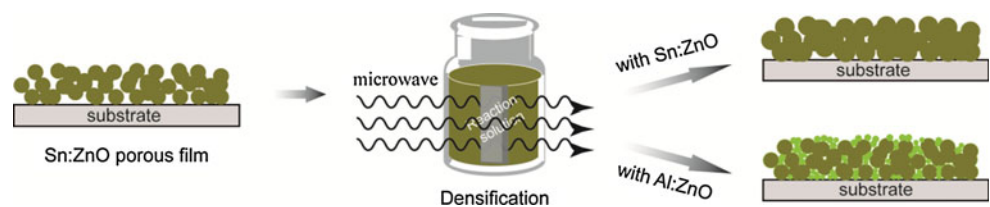
Fig. 3 SEM images of the surface (*left*) and cross section (*right*) of **a** SZO3-D1 and **b** SZO3-D2

Fig. 4 A schematic illustration of the microwave-assisted densification procedure

in the corresponding Sn:ZnO (SZO3F-D1) and Al:ZnO (SZO3F-D2) reaction solutions. The SZO3F-D1 film showed larger grains and was less dense than the SZO3F-D2 film. Because Sn:ZnO prefers to nucleate and grow on the surface of the particles and aggregates, this leads to large grains. On the other hand, the particle size of Sn:ZnO is relatively large (~ 18 nm) and therefore it is difficult for them to infiltrate the small pores. However, Al:ZnO prefers to form their own particles due to the lattice mismatch with respect to Sn:ZnO. Since the particle size of Al:ZnO is ~ 9 nm, which is much smaller than that of Sn:ZnO, they

can easily penetrate into the pores. Figure 4 illustrates these two densification mechanisms.

3.2 Electrical properties

The electrical resistivity, carrier concentration and Hall mobility of the Sn:ZnO films as a function of the initial dopant concentrations are plotted in Fig. 5. The resistivity of the films decreased with increasing dopant concentrations up to 7.5% (SZO3), where the film resistivity reached a minimum of 20.3 Ω cm. This decrease in resistivity was
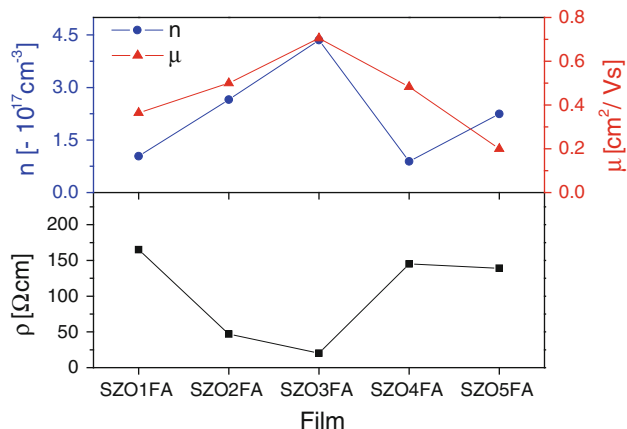
Fig. 5 Electrical resistivity (ρ), carrier concentration (n) and Hall mobility (μ) of Sn:ZnO films as a function of initial dopant concentrations
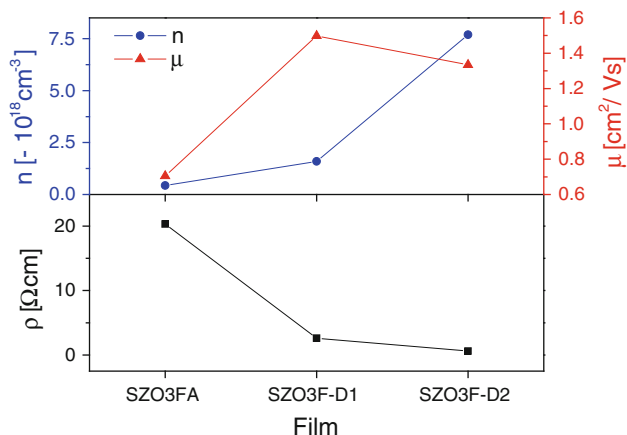

Fig. 6 Comparison of the electrical resistivity (ρ), carrier concentration (n) and Hall mobility (μ) of SZO3F films without and with the densification steps

a result of the increase of free carrier concentration and Hall mobility due to the donor electrons from the dopant. The resistivity of the films, however, increased with further increase of the dopant concentration, because the excess of Sn-doping decreased the carrier concentration and Hall mobility. Such a decrease of free carrier concentration is due to the excess of Sn-doping producing crystal disorders and defects which act as carrier traps rather than electron donors [42]. The Hall mobility of the films decreased as well with further increasing the dopant concentration. This decrease in mobility is associated with the decrease of the Sn:ZnO crystal size and thus increasing grain boundary scattering.

The electrical properties improved significantly after the densification steps. Figure 6 shows the dependence of the electrical resistivity, carrier concentration and Hall mobility of the SZO3F film after two different densification steps. Both carrier concentration and Hall mobility

increased after densification. As a result, the resistivity of SZO3F-D1 decreased from 20.3 to 2.6 Ω cm, and SZO3F-D2 to 0.6 Ω cm. It can be concluded that the microstructure (i.e., the density) of the films plays an important role in determining the electrical properties. The denser the film, the lower was its electrical resistivity.

3.3 Optical properties

Figure 7a shows the UV–Vis reflection spectra of the Sn:ZnO powders with the different initial dopant concentrations. If the thickness of the powder sample, t, is sufficiently large so that all incident light is absorbed or scattered before reaching the back surface of the sample, then the relationship between reflectance and absorption coefficient can be described using the following equation [39, 43]:

$$2\alpha t = \ln\left(\frac{R_{\max} - R_{\min}}{R - R_{\min}}\right) \tag{1}$$

where α is the absorption coefficient, $R_{\max}$ and $R_{\min}$ are the maximum and minimum reflectance in reflection spectra and R is the reflectance for any intermediate energy photons.

For the direct transition semiconductor, the optical band gap of the film, E_g, can be determined from the absorption coefficient of the materials using the following equation [44]:

$$\alpha h v = A\left(h v - E_g\right)^{1/2} \tag{2}$$

where A is a constant, h is the Planck's constant, and v is the frequency of the incident photon. Combining Eqs. 1 and 2, $\{\ln[(R_{\max} - R_{\min})/(R - R_{\min})]\}^2$ versus the energy is plotted in Fig. 7b. Extrapolation of the linear part of the absorption edge leads to the axis interception which corresponds to the band gap E_g. The band gap of all Sn:ZnO samples (between 3.22 and 3.25 eV) are slightly smaller than that of pure ZnO (3.25 eV). Similar results were reported for other doped ZnO samples [45–47]. The lack of Burstein-Moss effect [48] in our samples indicates that the Fermi level did not move into the conduction band after doping. The only small band gap variation of the Sn:ZnO samples is probably due to the small variation of the dopant concentration and the crystal size.

Figure 8 shows the optical transmittance spectra at room temperature for a 400-nm-thick SZO3 film densified with SZO3 reaction solution after different heat treatments. An average transmittance of 90% between 400 and 850 nm was obtained. The weak fluctuation in the spectrum is mainly due to interference between the top and bottom surface of the film. After annealing at 600 °C for 2 h in air, the average transmittance slightly increased to 91% mainly due to the removal of residual organics on the surface of
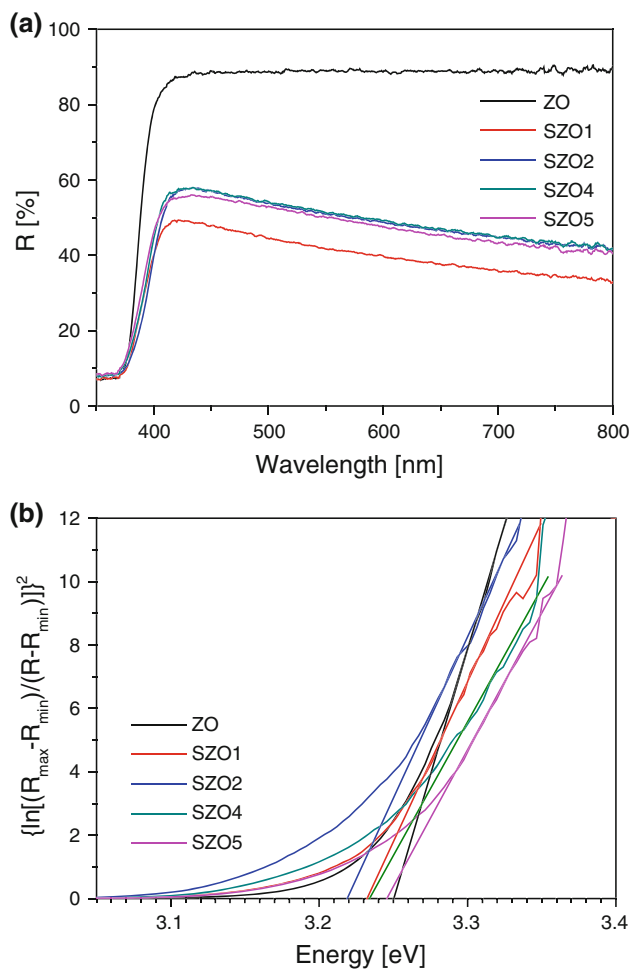
(a)

(b)

Fig. 7 **a** The UV–Vis reflection spectra of the Sn:ZnO powders, and **b** square of the absorption coefficient as a function of photo energy
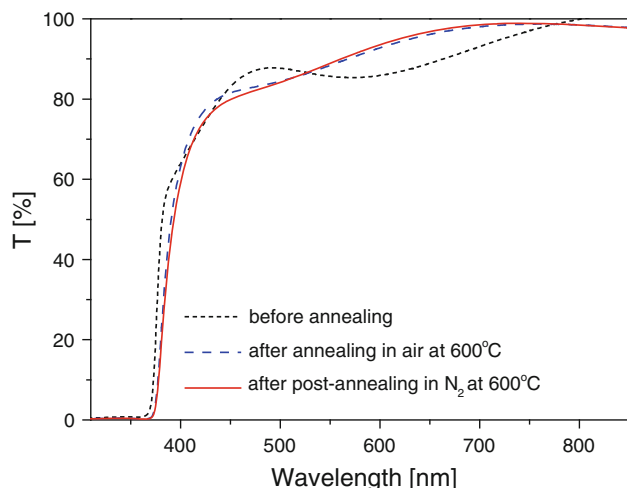

Fig. 8 Optical transmittance spectra of a 400-nm-thick SZO3 film densified with SZO3 reaction solution after different heat treatments

the particles. The red shift of the band gap could be explained by the growth of the crystal size (from 18 to 40 nm) due to the heat treatment. After post annealing in N_2, the optical transmittance of the film remained nearly the same.

4 Conclusions

The microwave-assisted non-aqueous sol–gel process is an efficient method for the synthesis of Sn:ZnO nanoparticles and for the densification of porous thin films. Phase pure and highly crystalline Sn:ZnO nanoparticles were obtained, and homogeneous Sn:ZnO films were successfully prepared on fused silica substrates by dip-coating from the respective nanoparticle dispersions. Although the final dopant concentration was much lower than the initial one, it is possible to vary it within a range that greatly affects the electrical properties of the films. A minimum resistivity of 20.3 Ω cm was obtained for a porous, non-densified SZO3 film after post-annealing under N_2. The resistivity of this film can be reduced to 0.6 Ω cm after densification with Al:ZnO nanoparticles. The average optical transmittance of a 400-nm-thick SZO3 film densified with SZO3 reaction solution after annealing in N_2 was 91%. It turned out that the heat treatment did not have any negative effect on the optical transmittance of the films. In addition, the combination of Sn:ZnO with Al:ZnO within the same film showed some improvement in the electrical properties in comparison with pure Sn:ZnO, suggesting that multicomponent films might represent promising candidates for new and improved TCOs.

References

1. Shishiyanu ST, Shishiyanu TS, Lupan OI (2005) Sens Actuators B 107:379–386
2. Gong H, Hu JQ, Wang JH, Ong CH, Zhu FR (2006) Sens Actuators B 115:247–251
3. Nanto H, Sokooshi H, Kawai T (1993) Sens Actuators B 14:715–717
4. Iwabuchi Y, Shiino O, Yoshikawa M, Kamei M (2007) Japan Patent JP2007311041-A, 29 Nov 2007
5. Minami T, Miyata T, Ohtani Y (2007) Phys Status Solidi A 204:3145–3151
6. Choi SE, Oh YT, Ham HK, Kim TW, Heo GS, Park JW, Choi BH, Shin DC (2011) Curr Appl Phys 11:S255–S257
7. Nam SH, Kim MH, Yoo DG, Jeong SH, Kim DY, Lee NE, Boo JH (2010) Surf Rev Lett 17:121–127
8. Hong JS, Kim SM, Park SJ, Choi HW, Kim KH (2010) Mol Cryst Liq Cryst 520:295–303

9. Yoo DG, Nam SH, Kim MH, Jeong SH, Jee HG, Lee HJ, Lee NE, Hong BY, Kim YJ, Jung D, Boo JH (2008) Surf Coat Technol 202:5476–5479

10. Park SHK, Ryu M, Hwang CS, Yang S, Byun C, Lee JI, Shin J, Yoon SM, Chu HY, Cho KI, Lee K, Oh MS, Im S (2008) Sid Int Symp Dig Tec 39:629–632

11. Granqvist CG (2007) Sol Energy Mater Sol Cells 91:1529–1598

12. Kang DW, Kuk SH, Ji KS, Lee HM, Han MK (2011) Sol Energy Mater Sol Cells 95:138–141

13. Kim D, Kim H, Jang K, Park S, Pillai K, Yi J (2011) J Electrochem Soc 158:D191–D195

14. Yoshida Y, Tanaka S, Hiromitsu I, Fujita Y, Yoshino K (2008) Jpn J Appl Phys 47:867–871

15. Sundaramoorthy R, Repins IL, Gennett T, Pern FJ, Albin D, Li JAV, DeHart C, Glynn S, Perkins JD, Ginley DS, Gessert T (2009) IEEE Phot Spec Conf 1–3:2225–2230

16. Cavani F, Trifiro F, Vaccari A (1991) Catal Today 11:173–301

17. Kurz A, Aegerter MA (2004) J Sol-Gel Sci Technol 31:267–271

18. Holmelund E, Schou J, Tougaard S, Larsen NB (2002) Appl Surf Sci 197:467–471

19. Kelly PJ, Zhou Y (2006) J Vac Sci Technol A 24:1782–1789

20. Bae SY, Na CW, Kang JH, Park J (2005) J Phys Chem B 109:2526–2531

21. Allah FK, Abe SY, Nunez CM, Khelil A, Cattin L, Morsli M, Bernede JC, Bougrine A, del Valle MA, Diaz FR (2007) Appl Surf Sci 253:9241–9247

22. Chen KJ, Hung FY, Chang SJ, Young SJ, Hu ZS, Chang SP (2010) J Sol-Gel Sci Technol 54:347–354

23. Kyaw AKK, Sun XW, Jiang CY (2009) J Sol-Gel Sci Technol 52:348–355

24. Goebbert C, Nonninger R, Aegerter MA, Schmidt H (1999) Thin Solid Films 351:79–84

25. Prodi-Schwab A, Luthge T, Jahn R, Herbig B, Lobmann P (2008) J Sol-Gel Sci Technol 47:68–73

26. Bilecka I, Djerdj I, Niederberger M (2008) Chem Commun 886–888

27. Bilecka I, Luo L, Djerdj I, Rossell MD, Jagodic M, Jaglicic Z, Masubuchi Y, Kikkawa S, Niederberger M (2011) J Phys Chem C 115:1484–1495

28. Tsaroucha M, Aksu Y, Irran E, Driess M (2011) Chem Mater 23:2428–2438

29. Coelho AA (2007) TOPAS-Academic V4.1. http://www.topas-academic.net/

30. Young RA (ed) (1993) The Rietveld Method. Oxford University Press, IUCr Book Series

31. Finger LW, Cox DE, Jephcoat AP (1994) J Appl Crystallogr 27:892–900

32. Dollase WA (1986) J Appl Crystallogr 19:267–272

33. Snyder RL, Bunge HJ, Fiala J (eds) (1999) Defect and microstructure analysis from diffraction. Oxford University Press, New York, pp 94–126

34. Balzar D, Audebrand N, Daymond MR, Fitch A, Hewat A, Langford JI, Le Bail A, Louer D, Masson O, McCowan CN, Popa NC, Stephens PW, Toby BH (2004) J Appl Crystallogr 37:911–924

35. McCusker LB, Von Dreele RB, Cox DE, Louer D, Scardi P (1999) J Appl Crystallogr 32:36–50

36. Pitschke W, Hermann H, Mattern N (1993) J Appl Crystallogr 26:132–134

37. Karvaly B, Hevesi I (1971) Z Naturforsch A Phys Sci 26:245–249

38. Wendlandt WW, Hecht HG (1966) Reflectance Spectroscopy. Wiley-Interscience, New York

39. Murphy AB (2007) Sol Energy Mater Sol Cells 91:1326–1337

40. Stroppa DG, Montoro LA, Beltran A, Conti TG, da Silva RO, Andres J, Longo E, Leite ER, Ramirez AJ (2009) J Am Chem Soc 131:14544–14548

41. Shannon RD (1976) Acta Crystallogr A 32:751–767

42. Hu JH, Gordon RG (1992) J Appl Phys 72:5381–5392

43. Kumar V, Sharma SK, Sharma TP, Singh V (1999) Opt Mater 12:115–119

44. Hamberg I, Granqvist CG (1986) J Appl Phys 60:R123–R159

45. Hammarberg E, Prodi-Schwab A, Feldmann C (2009) J Colloid Interface Sci 334:29–36

46. Yung KC, Liem H, Choy HS (2009) J Phys D Appl Phys 42:185002/1–5

47. Benelmadjat H, Boudine B, Halimi O, Sebais M (2009) Opt Laser Technol 41:630–633

48. Sernelius BE, Berggren KF, Jin ZC, Hamberg I, Granqvist CG (1988) Phys Rev B 37:10244–10248